The nearby extreme accretion and feedback system PDS 456: finding a complex radio-emitting nucleus

Monthly Notices of the ROYAL ASTRONOMICAL SOCIETY

MNRAS **500,** 2620–2626 (2021) doi:10.1093/mnras/staa2445
Advance Access publication 2020 August 17

The nearby extreme accretion and feedback system PDS 456: finding a complex radio-emitting nucleus

Jun Yang [1]★ Zsolt Paragi [2] Emanuele Nardini [3,4] Willem A. Baan [5] Lulu Fan [6,7,8]★ Prashanth Mohan [9] Eskil Varenius [1,10] and Tao An [9]

[1]*Onsala Space Observatory, Department of Space, Earth and Environment, Chalmers University of Technology, SE-439 92 Onsala, Sweden*
[2]*Joint Institute for VLBI ERIC (JIVE), Postbus 2, NL-7990 AA Dwingeloo, the Netherlands*
[3]*Dipartimento di Fisica e Astronomia, Università di Firenze, via G. Sansone 1, I-50019 Sesto Fiorentino, Firenze, Italy*
[4]*INAF – Osservatorio Astrofisico di Arcetri, Largo Enrico Fermi 5, I-50125 Firenze, Italy*
[5]*Netherlands Institute for Radio Astronomy (ASTRON), NL-7991 PD Dwingeloo, the Netherlands*
[6]*CAS Key Laboratory for Research in Galaxies and Cosmology, Department of Astronomy, University of Science and Technology of China, Hefei 230026, China*
[7]*School of Astronomy and Space Sciences, University of Science and Technology of China, Hefei 230026, China*
[8]*Shandong Provincial Key Lab of Optical Astronomy and Solar-Terrestrial Environment, Institute of Space Science, Shandong University, Weihai 264209, China*
[9]*Shanghai Astronomical Observatory, Key Laboratory of Radio Astronomy, Chinese Academy of Sciences, Shanghai 200030, China*
[10]*Jodrell Bank Centre for Astrophysics, The University of Manchester, Oxford Road, Manchester M13 9PL, UK*

Accepted 2020 August 11. Received 2020 July 28; in original form 2020 July 6

ABSTRACT

When a black hole accretes close to the Eddington limit, the astrophysical jet is often accompanied by radiatively driven, wide-aperture and mildly relativistic winds. Powerful winds can produce significant non-thermal radio emission via shocks. Among the nearby critical accretion quasars, PDS 456 has a very massive black hole (about 1 billion solar masses), shows a significant star-forming activity (about 70 solar masses per year), and hosts exceptionally energetic X-ray winds (power up to 20 per cent of the Eddington luminosity). To probe the radio activity in this extreme accretion and feedback system, we performed very long baseline interferometric (VLBI) observations of PDS 456 at 1.66 GHz with the European VLBI Network and the enhanced Multi-Element Remotely Linked Interferometry Network. We find a rarely seen complex radio-emitting nucleus consisting of a collimated jet and an extended non-thermal radio emission region. The diffuse emission region has a size of about 360 pc and a radio luminosity about three times higher than that of the nearby extreme starburst galaxy Arp 220. The powerful nuclear radio activity could result either from a relic jet with a peculiar geometry (nearly along the line of sight) or more likely from diffuse shocks formed naturally by the existing high-speed winds impacting on high-density star-forming regions.

Key words: galaxies: active – galaxies: jets – galaxies: nuclei – quasars: individual: PDS 456 – radio continuum: galaxies.

1 INTRODUCTION

Accreting supermassive black holes (SMBHs) can provide mechanical feedback on their host galaxies via launching jets and winds. Jets are collimated relativistic outflows emitting synchrotron emission (e.g. Blandford, Meier & Readhead 2019). Winds are non-jetted, relatively wider angled outflows with a relatively low speed of $\lesssim 0.3c$ (e.g. Tombesi 2016) and are mainly traced by optical and X-ray spectroscopic as well as radio continuum observations (e.g. Panessa et al. 2019). When the SMBHs have accretion rates approaching the Eddington limit, they may produce not only jets (e.g. Giroletti et al. 2017; Yang et al. 2019, 2020a) but also extremely powerful winds (e.g. Nardini et al. 2015; Tombesi et al. 2015; Fiore et al. 2017). These winds can sweep out the interstellar medium (e.g. Zakamska & Greene 2014), produce radio-emitting shocks (e.g. Nims, Quataert & Faucher-Giguère 2015), contribute the extragalactic gamma-ray background (e.g. Lamastra et al. 2017), and quench star formation (e.g. Kormendy & Ho 2013; Fiore et al. 2017). Observing this complex nuclear radio activity with the very long baseline interferometric (VLBI) imaging technique can provide information to constrain physical properties in the extreme accreting environment and help understand feedback with the host galaxy.

The quasar PDS 456 (IRAS 17254−1413) at a redshift of $z = 0.184$ is the most luminous quasar in the local ($z < 0.3$) Universe (Torres et al. 1997; Simpson et al. 1999). The quasar has a bolometric luminosity $L_{\rm bol} \sim 10^{47}$ erg s^{-1} (Reeves et al. 2000) comparable to its Eddington luminosity $L_{\rm Edd} \sim 1.3 \times 10^{47}$ erg s^{-1} (Nardini et al. 2015) and a disc geometry close to face-on (Yun et al. 2004; Bischetti et al. 2019). It is also an ultraluminous infrared (IR) galaxy (ULIRG) with a luminosity of $L_{\rm FIR} = 1.3 \times 10^{12}$ L$_\odot$ (Yun et al. 2004). Compared to the known nearby critical accretion systems, its central SMBH has

★ E-mail: jun.yang@chalmers.se (JY); llfan@ustc.edu.cn (LF)

Table 1. Summary of the VLBI observations of PDS 456 at 1.66 GHz.

Observing date and time (UT)	Participating stations
2018 Mar 28, 02 h 30 m–08 h 30 m	Jb, Wb, Ef, Mc, On, Tr, Hh
2020 Jan 22, 06 h 30 m–13 h 00 m	Jb, Wb, Ef, On, Tr, Hh, Ir, Sr, Kn, Da, Pi, Cm, De

the highest mass, $M_{\rm bh} = 10^{9.2\pm0.2}$ $M_\odot$ (see supplementary material in Nardini et al. 2015).

As a critical accretion system, PDS 456 is of great interest for probing powerful multiphase winds and outflows. It hosts a quasi-spherical mildly relativistic ($\lesssim 0.3c$) X-ray wind with a very high kinetic energy of $\sim 0.2 L_{\rm Edd}$ (Nardini et al. 2015). The power of X-ray winds positively correlates with the X-ray luminosity, and thus these winds are likely radiation pressure driven (Matzeu et al. 2017). From soft X-ray (Boissay-Malaquin et al. 2019; Reeves et al. 2020) to ultraviolet (O'Brien et al. 2005; Hamann et al. 2018) bands, there are also more reports of highly blueshifted absorption lines at velocities consistent with the hard X-ray winds. Moreover, the CO (3–2) emission line observations at ∼1 mm show that there exist not only some spatially extended molecular outflows up to ∼5 kpc but also high-velocity (∼800 km s^{-1}) compact outflows in the nucleus (Bischetti et al. 2019).

Based on the multiwavelength spectral energy distribution (SED), PDS 456 is a radio-quiet analogue of the well-known radio-loud blazar 3C 273 (Yun et al. 2004). The radio counterpart of PDS 456 is a steep-spectrum source (Yun et al. 2004) with a flux density of 25 ± 4 mJy at 1 GHz and a spectral index of $\alpha = -0.84 \pm 0.11$ (Yang et al. 2019). Besides the intense active galactic nucleus (AGN), its SED in the far-IR shows evidence for significant star-forming activity in its host galaxy (Yun et al. 2004). The radio emission is likely dominated by the AGN activity (Yun et al. 2004). The pilot high-resolution VLBI observations at 5 GHz found a faint jet structure consisting of a few components on the deca-pc scale in the nuclear region, while failed to image some very diffuse radio structure (∼70 per cent of its total flux density; Yang et al. 2019). To get a complete view of the potential large-scale radio activity that may owe to an episodic jet, and understand nuclear starbursts and/or wind shocks, we performed new VLBI imaging observations at a suitable frequency of 1.66 GHz with the European VLBI Network (EVN) plus the enhanced Multi-Element Remotely Linked Interferometry Network (e-MERLIN).

This paper is organized as follows: We describe the VLBI observations and the data reduction in Section 2 and present the imaging results of PDS 456 in Section 3. We discuss star formation rate (SFR) based on the IR SED, physical characteristics of the observed complex nuclear radio activity and potential identification with the jet, starburst, and shock activity, and the accretion rate in Section 4. Throughout the paper, a standard Lambda cold dark matter cosmological model with $H_0 = 71$ km s^{-1} Mpc^{-1}, $\Omega_{\rm m} = 0.27$, and $\Omega_\Lambda = 0.73$ is adopted; the images then have a scale of 3.1 pc mas^{-1}.

2 OBSERVATIONS AND DATA REDUCTION

Table 1 gives a summary of our VLBI observations at 1.66 GHz. At first, we observed PDS 456 with the EVN on 2018 March 28. Owing to a severe instrumental problem with the digital filters, the target was reobserved with the EVN plus the e-MERLIN on 2020 January 22. In the two experiments, the participating stations were Jodrell Bank MK II (Jb), Westerbork single antenna (Wb), Effelsberg (Ef), Medicina (Mc), Onsala (On), Toruń (Tr), Hartebeesthoek (Hh), Irebene (Ir), Sardinia (Sr), Knockin (Kn), Darnhall (Da), Pickmere (Pi), Cambridge (Cm), and Defford (De).

Both observations were carried out in the e-VLBI mode. The data transfer speeds were 1024 Mbps (16 subbands in dual polarization, 16 MHz per subband, 2-bit quantization) at the EVN stations and 512 Mbps (2 subbands in dual polarization, 64 MHz per subband, 2-bit quantization) at the e-MERLIN stations (Kn, Da, Pi, Cm, and De). The data correlation was done in real time by the EVN software correlator (SFXC; Keimpema et al. 2015) at JIVE (Joint Institute for VLBI, ERIC) using an integration time of 1 s and a frequency resolution of 1 MHz.

The observations of the faint source PDS 456 applied the phase-referencing observing technique. The pc-scale compact source J1724−1443 (Petrov et al. 2006), about 59 arcmin apart from our target, was used as the phase-referencing calibrator. Its J2000 position is RA = $17^{\rm h}24^{\rm m}46\overset{\rm s}{.}96654$ ($\sigma_{\rm ra} = 0.1$ mas), Dec. = $-14^\circ43'59\overset{''}{.}7609$ ($\sigma_{\rm dec} = 0.2$ mas) in the source catalogue 2016a from the Goddard Space Flight Centre VLBI group. The cycle time of the periodic nodding observations was about 4 min (∼0.5 min for J1724−1443, ∼2.5 min for PDS 456, and ∼1.0 min for two gaps). A very bright flat-spectrum radio quasar NRAO 530 (J1733−1304; e.g. An et al. 2013) was also observed to determine the instrumental phases and bandpass shapes.

The data were calibrated using the National Radio Astronomy Observatory (NRAO) software package Astronomical Image Processing System (AIPS; Greisen 2003). First, we reviewed the data carefully and flagged out off-source data and some very low sensitivity data. Secondly, we ran a priori amplitude calibration with properly smoothed antenna monitoring data (system temperatures and gain curves) or nominal system equivalent flux densities when these monitoring data were not available. Thirdly, we updated the position of the antenna Sr with the AIPS task CLCOR (options ANAX and ANTP) according to the first geodetic VLBI measurements (project code EL054, reported by Leonid Petrov on the web)[1]: J2000 epoch, position: $(X, Y, Z) = (+4865\,183.542, +791\,922.255, +4035\,136.024)$ m, velocity: $(V_{\rm x}, V_{\rm y}, V_{\rm z}) = (-12.15, +19.29, +10.86)$ mm yr^{-1}, and axis offset: 0.031 m. The corrections are $(\Delta X, \Delta Y, \Delta Z) = (+0.6116, -0.1553, -1.0446)$ m for the antenna position and +0.031 m for the antenna axis offset. Fourthly, the general bootstrap phase calibrations were performed. We corrected the ionospheric dispersive delays according to the maps of total electron content provided by global positioning system satellite observations, removed phase errors due to the antenna parallactic angle variations, and aligned the phases across the subbands via running fringe fitting with a 2-min scan of the NRAO 530 data. After these calibrations, we combined all the subbands, ran the fringe fitting, and applied the solutions to PDS 456 by interpolation. Finally, the bandpass calibration was performed. All the above steps were scripted in the ParselTongue interface (Kettenis et al. 2006).

We first imaged the phase-referencing source J1724−1443. The imaging procedure was performed through a number of iterations of model fitting with a group of delta functions, i.e. point-source models,

[1] http://astrogeo.org/petrov/discussion/el054/

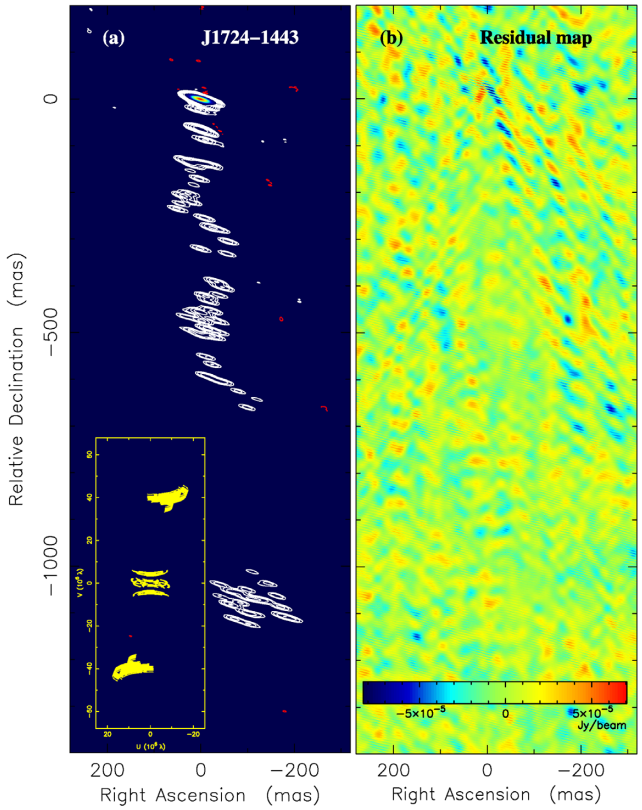

Figure 1. The point-source model fitting results of the visibility data of the calibrator J1724−1443. (a) The high-dynamic-range map of its complex jet structure. The full width at half-maximum (FWHM) of the synthesized beam is 29.6 mas × 6.6 mas at 73.9°. The contours are 0.05 × (−1, 1, 2, ..., 64) mJy per beam. The image peak is 229 mJy per beam. With respect to the image noise level 0.017 mJy per beam, the dynamic range reaches 13 740. The inset plots the non-optimal (u, v) coverage. (b) The noise distribution in the residual map. The display range is between −0.083 and +0.070 mJy per beam.

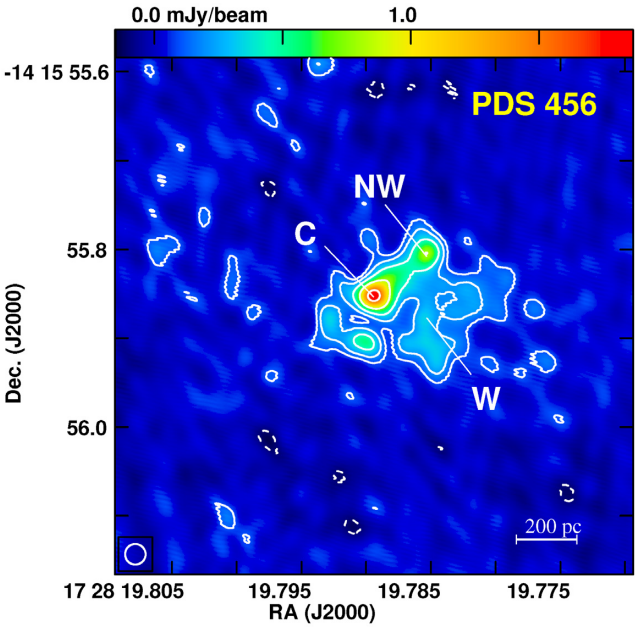

Figure 2. The total intensity image of the quasar PDS 456 observed by the EVN plus e-MERLIN at 1.66 GHz. A circular restoring beam with an FWHM = 23 mas is used. The contours start from 0.1 mJy per beam (3σ) and increase by a factor of −1, 1, 2, 4, 8, and 16.

and the self-calibration in DIFMAP (Shepherd, Pearson & Taylor 1994). This is similar to the non-negative least-squares algorithm (Briggs 1995) in the image plane and thus can also allow users to achieve a high-dynamic-range map (Yang et al. 2020b). We reran the fringe fitting and the amplitude and phase self-calibration in AIPS with the input source model made in DIFMAP. All these solutions were also transferred to the data of PDS 456 by the linear interpolation.

The total intensity and residual maps from the direct model fitting are shown in Fig. 1. The calibrator J1724−1443 has a single-sided core-jet structure with a total flux density of 0.27 ± 0.02 Jy. Its radio core has a flux density of 0.23 ± 0.01 Jy and is used as the reference point in the phase-referencing calibration. There were 79 point-source models used in the Stokes I map. Both the Stoke I and zero-flux density V maps have almost the same off-source noise level, $\sigma_{\rm rms}$ = 0.017 mJy per beam. The noise distribution in the residual map of Stokes I is quite uniform in particular in the on-source region, although there is only one station (Hh) on the long baselines. Because the method tried to use the minimum number of point sources and the (u, v) coverage is poor, the faint jet structure does not look very smooth. The e-MERLIN data were excluded in the final image because they gave some low-level noise peaks (∼0.15 mJy per beam, ∼0.07 per cent of the peak brightness) in the residual map.

We imaged the faint target PDS 456 without any self-calibration in DIFMAP. First, we made a low-resolution CLEAN map with the e-MERLIN and Jb. The target PDS 456 has a peak brightness of 7.6 ± 0.2 mJy per beam using natural weighting [beam FWHM: 506 × 111 mas^2 in position angle (PA) 14°], and indicates a slightly resolved structure with a total flux density of 12.3 ± 0.3 mJy and a deconvolved size of ∼123 mas. After the deconvolution of the major component with a proper window, there is a hint of two-sided jet-like structure at PAs of about −25° and +145° in the residual map but they are not bright enough (<5σ) for a confirmation as real features. This is followed up by making a high-resolution map with the EVN plus e-MERLIN data. We used σ^{-2} (σ, data error) as the visibility data weight and the purely natural grid weighting to clean the diffuse emission (peak brightness: 0.23 mJy per beam) in the nuclear region. Owing to residual phase errors of the phase-referencing calibration, our final image has a noise level about a factor of 2 higher than the statistical value estimated in the zero-flux Stokes V map.

3 EVN PLUS E-MERLIN IMAGING RESULTS

The total intensity maps of PDS 456 observed with the EVN plus the e-MERLIN on 2020 January 22 are shown in Fig. 2. The beam synthesized with natural weighting has an FWHM of 23 × 5.2 mas^2 in PA = +73°. To avoid resolving out diffuse radio features, we artificially increased the beam area and used a circular beam with an FWHM of 23 mas in the map. The nucleus of PDS 456 consists of two relatively compact knots, denoted as the components C and NW, and a diffuse emission region extending mainly towards west and south. According to the position of its centroid, we labelled the complex structure as the component W. The unshown image from the first epoch observation has a significantly lower quality owing to the limited telescopes and sensitivity, yet it independently confirms the existence of the components C, NW, and W. The relatively bright-spot at ∼12σ in the south, Fig. 2, was only marginally (∼3σ) detected in the early epoch.

Table 2. Summary of characteristic parameters of the radio components detected in PDS 456. Columns give (1) component name, (2) total flux density, (3 and 4) relative offsets in right ascension and declination with respect to the peak component C, (5) best-fitting size $\theta_{\rm size}$ of the circular Gaussian model, (6) brightness temperature $T_{\rm b}$, and (7) radio luminosity $L_{\rm R}$.

Name	$S_{\rm int}$ (mJy)	$\delta_{\rm ra}$ (mas)	$\delta_{\rm dec}$ (mas)	$\theta_{\rm size}$ (mas)	$\log T_{\rm b}$ (K)	$\log L_{\rm R}$ (erg s^{-1})
C	2.31 ± 0.03	+0.0 ± 0.1	+0.0 ± 0.1	11.1 ± 0.4	6.99 ± 0.05	39.60 ± 0.04
NW	1.15 ± 0.03	−62.7 ± 0.2	+48.8 ± 0.2	14.7 ± 0.7	6.45 ± 0.06	39.30 ± 0.04
W	8.18 ± 0.14	−46.3 ± 0.9	−11.0 ± 0.8	118.6 ± 1.6	5.48 ± 0.05	40.15 ± 0.04

The circular Gaussian model fitting results in DIFMAP (version 2.5e) are given in Table 2. All the errors are formal uncertainties measured at the reduced $\chi^2 = 1$. Empirically, the flux density measurements have a systematic error of around 10 per cent. Compared to the flux density (16 ± 2 mJy at 1.66 GHz) predicted by its radio spectrum (Yang et al. 2019), the VLBI map only restores ∼70 per cent. With respect to J1724−1443, the differential astrometry gives a J2000 position of RA = $17^{\rm h}28^{\rm m}19\overset{\rm s}{.}78958$ and Dec. = $-14^\circ15'55\overset{''}{.}8520$ for the peak component C. This is in agreement with the average position of components C1 and C2 at 5 GHz reported by Yang et al. (2019) if we consider significant systematic error due to the extended source structure and the different (u, v) coverage, $\sim 0.1\theta_{\rm size}$ (∼1 mas). With respect to the component C, we reported the relative offsets of components NW and W in Table 2.

In the last two columns of Table 2, we also report radio luminosity $L_{\rm R} = \nu L_\nu$ (ν, observing frequency) and brightness temperature $T_{\rm b}$, estimated (e.g. Condon et al. 1982) as

$$T_{\rm b} = 1.22 \times 10^9 \frac{S_{\rm int}}{\nu_{\rm obs}^2 \theta_{\rm size}^2}(1+z), \quad (1)$$

where $S_{\rm int}$ is the integrated flux density in mJy, $\nu_{\rm obs}$ is the observation frequency in GHz, $\theta_{\rm size}$ is the FWHM of the circular Gaussian model in mas, and z is the redshift. The peak component C has a brightness temperature of $\sim 1 \times 10^7$ K. The very extended component W has a brightness temperature of $\sim 3 \times 10^5$ K.

4 DISCUSSION

4.1 SFR based on IR photometries

To estimate the SFR of PDS 456, we constructed the IR SED based on the multiband photometries in the literature. The photometries of the *Wide-field Infrared Survey Explorer* (*WISE*), the *Infrared Astronomical Satellite* (*IRAS*), the *Infrared Space Observatory*, and the James Clerk Maxwell Telescope Submillimetre Common-User Bolometer Array 2 have been retrieved from the NASA/IPAC Extragalactic Database. The *Herschel* photometries have been obtained by using the Herschel Interactive Processing Environment (HIPE v15.0.1). Compared to the previous SFR estimate based on SED fitting by Yun et al. (2004), we add two *WISE* bands at 12 and 22 μm, two *Herschel* PACS (Photodetector Array Camera and Spectrometer) bands at 70 and 160 μm, and three SPIRE (Spectral and Photometric Imaging REceiver) bands at 250, 350, and 500 μm. The inclusion of the *Herschel* PACS and SPIRE photometry is crucial for the SFR estimate as they map the cold dust emission peaking at 100–200 μm, which is directly involved in the star formation activity. We use the Bayesian SED modelling and interpreting code BAYESED (Han & Han 2012, 2014, 2019) to decompose the IR SED by using an AGN torus model and a simple modified blackbody model to represent the contribution from cold dust emission heated by a young stellar population (for more details, see Fan et al. 2016, 2017, 2019).

The derived IR luminosity of cold dust is $\sim 6.9 \times 10^{11}$ L$_\odot$, which is lower than that of Yun et al. (2004) by a factor of about 2. The difference is mainly due to the following two factors. First, our SED included the more data points at far-IR wavelengths than that of Yun et al. (2004). Secondly, we excluded the contribution of the AGN torus emission in the IR luminosity estimate. We convert the derived IR luminosity of cold dust into an SFR of about 69 M$_\odot$ yr^{-1}, assuming a Chabrier initial mass function (Chabrier 2003). We note that this SFR estimate should be taken as an upper limit due to source blending in the IR bands. The SFR is also in agreement with the results reported by Bischetti et al. (2019), suggesting significant but no extreme star-forming activity in the host galaxy.

4.2 Complex nuclear radio activity

The sub-kpc-scale radio nucleus of PDS 456 shows a complex radio morphology. This is not unusual in ultraviolet to sub-mm luminous but radio-weak/quiet sources because their radio emission originates from multiple physical mechanisms including low-radio-power jets, starbursts, and shocks (e.g. Panessa et al. 2019). Owing to the absence of bright radio cores and the missing of sensitive short baselines, VLBI observations of the radio counterparts of these galaxies often show non-detections or significantly overresolved radio structures. These cases involve extreme UV-selected starburst galaxies (Alexandroff et al. 2012), ULIRG IRAS 23365+3604 (Romero-Cañizales, Pérez-Torres & Alberdi 2012), hot dust-obscured galaxies (Frey et al. 2016), and sub-millimetre-selected galaxies (Chen et al. 2020).

4.2.1 Location of the radio core

The peak component C is the most promising component hosting the radio core of PDS 456. As the only central feature in the radio emission distribution, it is quite close to the optical centroid (J2000, R.A. = $17^{\rm h}28^{\rm m}19\overset{\rm s}{.}789380$, Dec. = $-14^\circ15'55\overset{''}{.}85543$, $\sigma_{\rm p}$ = 0.04 mas) reported by the *Gaia* astrometry (DR2; Gaia Collaboration 2018) using a point-source model. The small offset (radius ∼4.5 mas) is very likely due to a double-peaked optical brightness distribution (peak separation ∼0.22 kpc; Letawe, Letawe & Magain 2010). The component C might have a relatively hard spectrum. Assuming no significant flux density variability between the previous EVN observations at 5 GHz (Yang et al. 2019) and the new observations at 1.6 GHz, it has a spectral index of $\alpha = -0.5 \pm 0.1$.

4.2.2 Evidence of a low-radio-power jet

There exists some faint emission smoothly connecting the components C and NW. The component NW could represent the head of a jet along PA $\sim -52^{\circ}.1$. With respect to the component C, the apparent jet opening angle for the component NW is $\sim 10^{\circ}.7$. This is about a factor of 2 smaller than the median value of $21^{\circ}.5$ found in significantly beamed AGN jets (Pushkarev et al. 2017). Thus, the jet is unlikely to be very close to the line of sight. Assuming that the jet is close to the kinematic axis of the molecular disc (Bischetti et al. 2019), the jet viewing angle is $\theta_{\rm view} = 25^{\circ} \pm 10^{\circ}$. This indicates a de-projected length of 570 ± 20 pc for the component NW. Since there is no highly relativistic jet observed among extreme accretion systems (Yang et al. 2020a), the jet in PDS 456 might not be significantly Doppler boosted. Based on its low radio luminosity, it can be identified as a low-radio-power jet (e.g. Kunert-Bajraszewska et al. 2010; An & Baan 2012).

The component NW has also been marginally detected as the component X2 in the previous EVN observations at 5 GHz (Yang et al. 2019). The two observations give a spectral index of $\alpha = -0.8 \pm 0.1$. Owing to the near-face-on disc geometry (Bischetti et al. 2019) and the southern diffuse emission, only the jet on the approaching side is clearly identified. In the VLBI image at 1.6 GHz, we failed to confirm the existence of the component X1 (relative offsets, $\delta_{\rm ra} \approx 37.4$ mas, $\delta_{\rm dec} \approx -99.4$ mas), which was tentatively detected based on the shortest baseline of Ef–Wb on the receding side in the early observations at 5 GHz. Thus, the component X1 is probably an instrumental noise peak.

4.2.3 Diffuse component W: a relic jet or a composite of starbursts and shocks

PDS 456 has an optically thin integrated spectrum up to >15 GHz (Yang et al. 2019). As the component W contributes about half of the total radio emission of PDS 456 and the components C has a relatively hard spectrum, the component W may have a similar optically thin spectrum originating from non-thermal radio activity.

It is hard to naturally identify the component W as a jet component extending further from the component NW, as W has a diffuse radio morphology and a rather different extension direction from the existing jet, and there is no hint of a bending point. With respect to the component C, the component W shows a very wide angle (>180°) extension with a size of 118 ± 2 mas (366 ± 6 pc) and a centroid in PA $\sim -103^{\circ}$.

The component W may be an extended relic jet component close to the line of sight. Due to the peculiar jet geometry, the projected structure does not resemble an elongated jet. Compared to the inferred jet component NW, the identification necessitates a significant change in the jet direction. Currently, this information is unavailable.

Because of its high luminosity and extended morphology, it cannot be simply explained as a single supernova or a supernova remnant, which have typical peak monochromatic luminosities only up to $L_{\rm R} \sim 10^{38.7}$ erg s^{-1} (Weiler et al. 2002) and might only explain the brightened spot in the south. It is also hard to explain the component W as a group of supernovae and supernova remnants, i.e. starbursts. The nearby extreme starburst galaxy Arp 220 has an SFR of $\sim$220 M$_{\odot}$ yr^{-1} and a radio luminosity of 4×10^{39} erg s^{-1} (Varenius et al. 2016, 2019). Compared to Arp 220, PDS 456 has at least three times lower SFR (cf. Section 4.1). Assuming that 50 per cent of radio emission is from the starburst activity, the SFR derived based on the radio luminosity (equation 6, Bell 2003) would be 690 ± 70 M$_{\odot}$ yr^{-1}. This is inconsistent with the SED-based SFR and thus requires an additional source of energy injection.

Powerful high-speed AGN winds and outflows can naturally produce the additional synchrotron radio emission via shocks on scales of $\gtrsim$100 pc in the nuclear high-density star-forming region (e.g. Zakamska & Greene 2014; Nims et al. 2015). Mildly relativistic and wide-opening-angle winds have been identified in X-ray spectroscopic observations (e.g. Nardini et al. 2015; Matzeu et al. 2017; Reeves et al. 2020), with reports of multiple velocity components, up to 0.46c (Reeves et al. 2018). A possible ultraviolet outflow at 0.3c has also been reported by Hamann et al. (2018). Thus, mildly relativistic winds can extend farther out to pc scale (Reeves et al. 2020), as also inferred from Section 4.3 and thus might have a large impact on the whole nuclear region. Two CO(3–2) molecular outflow components were identified by Bischetti et al. (2019) in the compact nuclear region. One is a blueshifted, high-velocity ($v \sim -800$ km s^{-1} outflow component. The other is a low-velocity ($\lesssim$500 km s^{-1}), high-velocity dispersion (peak: 360 km s^{-1}) outflow component, which is $\sim$50 mas west from the quasar and spatially coincident with the centroid of the radio component W. The coincidence agrees with the shock model.

The latter scenario involving shocks due to wind interaction is now probed further to estimate the SFR. This involves driving of galactic winds and consequent feedback with the host galaxy through star formation. The relevant forces in action on cold gas clouds (temperature $\leq 10^4$ K) at pc–kpc scales include ram pressure from hot outflowing gas (in which the cold clouds are embedded) and radiation pressure from the galactic disc, which are in opposition to the gravitational force due to the self-gravitating region of the disc (e.g. Sharma & Nath 2012); the corresponding SFR is approximated in terms of the wind velocity $v_{\rm w}$ and the circular velocity of the galactic disc $v_{\rm c}$

$$\mathrm{SFR} = (0.89\ \mathrm{M}_{\odot}\ \mathrm{yr}^{-1}) \left(\frac{v_{\rm w}}{v_{\rm c}}\right)^{5/2} \left(\frac{v_{\rm c}}{120\ \mathrm{km\ s}^{-1}}\right)^{25/8}. \quad (2)$$

For the above estimated $v_{\rm w}$ of 360–800 km s^{-1} and a fiducial value of $v_{\rm c} = 120$ km s^{-1}, the SFR is 13.9–102.1 M$_{\odot}$ yr^{-1}. As this range is consistent with the estimated 69 M$_{\odot}$ yr^{-1} from the IR observations, the latter is preferred.

If the component W is associated with the nuclear molecular outflows, and formed by the AGN winds sweeping up the high-density star-forming region, the energy conversion efficiency is $\frac{L_{\rm R}}{L_{\rm bol}} \sim 10^{-7}$. This is two orders of magnitude lower than that predicted by the model of spherical wind shocks (Nims et al. 2015). However, this might be acceptable for PDS 456 as the nuclear winds can preferentially propagate along the low-density polar directions. Our estimate is also consistent with the study of Zakamska & Greene (2014) that finds a strong association between powerful outflows and the radio luminosity in radio-quiet quasars, with a statistical median conversion efficiency of $\frac{L_{\rm R}}{L_{\rm bol}} \sim 10^{-6}$.

4.3 Wind velocity and the Eddington ratio

If the powerful wide-angle X-ray winds (Nardini et al. 2015) are radiatively driven (Matzeu et al. 2017), PDS 456 might have a super-Eddington accretion rate. The Eddington ratio $\Gamma_{\rm e}$ is the ratio of the accretion disc luminosity ($L_{\rm disc}$) to the Eddington luminosity ($L_{\rm Edd}$). For an optically thick geometrically thin disc (Shakura & Sunyaev 1973) in the vicinity of the SMBH,

$$\Gamma_{\rm e} = \frac{L_{\rm disc}}{L_{\rm Edd}} \approx \frac{1}{L_{\rm Edd}} \frac{G M_{\rm bh} \dot{M}}{2 r_{\rm bh}} = \frac{\dot{m}}{12\epsilon}, \quad (3)$$

where $M_{\rm bh}$ is the SMBH mass, $\dot{M}$ is the accretion rate and $\dot{m}$ is the accretion rate scaled in terms of the Eddington rate $\dot{M}_{\rm Edd}$, $L_{\rm Edd} = \epsilon \dot{M}_{\rm Edd} c^2$, where ϵ is the efficiency factor, and $r_{\rm bh} = 6\, r_{\rm G} = 6\, GM_{\rm bh}/c^2$ ($r_{\rm G}$ is the gravitational radius) is the assumed distance from which the radiation is assumed to peak and corresponds to the innermost stable circular orbit for a Schwarzschild black hole (non-rotating). The evolution of velocity of a free particle driven by radiation pressure from the inner disc is given by (e.g. Abramowicz, Ellis & Lanza 1990; Mohan & Mangalam 2015)

$$\frac{{\rm d}\beta}{{\rm d}x} = \frac{(1-\beta^2)}{2x^2\beta\xi}\left(\frac{\Gamma_{\rm e}\xi_{\rm s}^{1/2}}{(1-\beta^2)^{1/2}\xi^{1/2}}\left(1+\beta^2-\frac{8}{3}\beta\right)-1\right), \qquad (4)$$

where $x = r/r_{\rm G}$, $\xi = (1 - 1/x)$, and $\xi_{\rm s} = \xi(x = 6)$ and we have assumed a radial particle trajectory that is shown to be the case for the large-distance regime (Mohan & Mangalam 2015). The formulation corresponds to a wide-angle wind outflow launched from the innermost region subject to a radiative deceleration (an effective drag force), aided by the gravitational potential of the black hole. This can be used to estimate the Eddington ratio corresponding to an observed asymptotic wind velocity at the sub-pc–pc scale.

The equation (4) is solved assuming $\epsilon = 0.1$ and $\Gamma_{\rm e} = 0.1$–10.0 (sub- to super-Eddington luminosity), which corresponds to $\dot{m} = 0.12$–12.0 using equation (3). For a Keplerian angular velocity $\Omega_{\rm bh} = GM_{\rm bh}/r_{\rm bh}^3$ associated with the launch radius $r_{\rm bh}$, the rotational velocity $v_\phi = r_{\rm bh}\Omega_{\rm bh} = c/6^{1/2} \approx 0.41\ c$. This could represent the minimum velocity of disc material that is advected into the winds and possibly into the collimated jet; for the boundary condition associated with equation (4), we assume an initial launch velocity $\beta(r_{\rm bh}) = 0.41$. A launch velocity exceeding $0.41c$ could indicate a poloidal component away from the disc plane and hint at mechanisms driving the material into trajectories away from the canonical Keplerian disc orbits, including a truncated disc scenario with a magnetically arrested disc accretion in the innermost region (e.g. Tchekhovskoy, Narayan & McKinney 2011) and energy extraction from the spin of the black hole (Blandford & Znajek 1977; Blandford & Payne 1982).

The above formulation can be generalized to estimate the velocity (or Lorentz factor) in the launching region for sources that indicate accretion rates near or exceeding the Eddington rate. The contours of the asymptotic velocity $\beta(\Gamma_{\rm e}, x)$ are plotted in Fig. 3. The particle velocity tends to a constant by $\approx$1000 $r_{\rm G} \approx 0.1$ pc (in the AGN rest frame). With an increase in $\Gamma_{\rm e}$, the velocity saturates to a larger value for the assumed $\beta(r_{\rm bh})$. Wind velocities of $\leq 0.3\ c$, as suggested by the radio and X-ray observations, can originate from the inner disc. These can be achieved well in advance and stay at the saturated value up to the pc scale and possibly beyond. The Eddington ratio corresponding to $\beta \leq 0.3c$ is $\Gamma_{\rm e} \leq 2.6$ ($\dot{M} \leq 71.3\ {\rm M}_\odot\ {\rm yr}^{-1}$), indicating that PDS 456 likely accretes at rates exceeding the Eddington rate. The estimated $\Gamma_{\rm e} \leq 2.6$ suggests that the bolometric luminosity (Reeves et al. 2000) may have been slightly underestimated (up to 3×10^{47} erg s^{-1}) or the SMBH mass (Nardini et al. 2015) may have been overestimated ($M_{\rm bh}$ as low as $3 \times 10^8\ {\rm M}_\odot$).

The formulation can act in an independent manner of constraining the Eddington ratio (and the associated accretion rate) in this and similar super-Eddington sources using the observed wind velocity as an input.

5 CONCLUSIONS

The luminous radio-quiet quasar PDS 456 is a nearby extreme accretion and feedback system. With the EVN plus e-MERLIN observations at 1.66 GHz, we achieved a more complete view of its complex radio morphology. Our VLBI images revealed a complex radio-emitting nucleus consisting of a collimated jet and a very extended structure. The latter has a size of about 120 mas and a radio luminosity about three times higher than that of the nearby extreme starburst galaxy Arp 220. The powerful nuclear radio activity could be explained as a relic jet with an unusual jet geometry or a more natural consequence of star-forming activity plus AGN-driven wind shocks. In addition, fainter nuclear radio activity and a sub-mJy flat-spectrum jet base may exist. The observed relativistic X-ray winds of $\sim$0.3c in the inner sub-pc-scale region suggest that PDS 456 likely accretes exceeding the Eddington rate. Future multifrequency deep VLBI observations of PDS 456 can potentially provide more details on the complex nuclear activity.

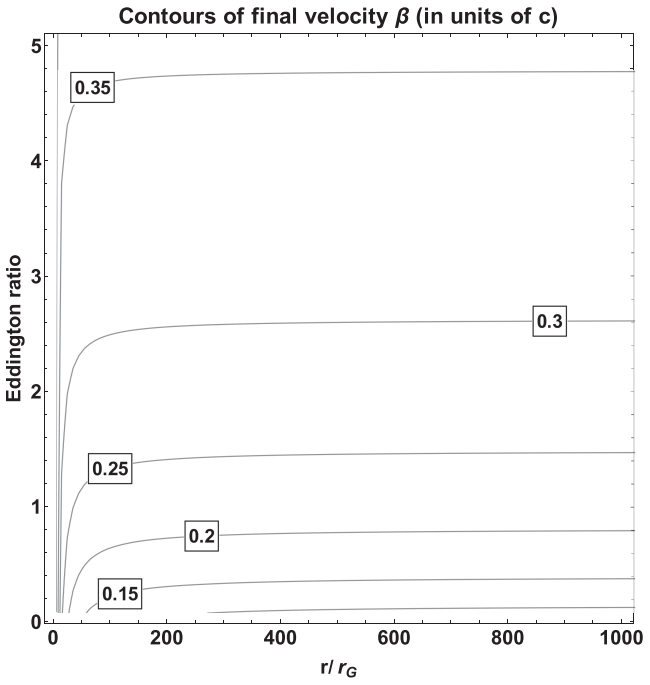

Figure 3. Contours of velocity β from equation (4) as a function of the Eddington ratio and the distance from the SMBH $r/r_{\rm G}$ (up to 1000, about 0.1 pc). The β values tend to a constant before about 0.1 pc for an initial launch velocity of 0.41 c. The radiatively driven and mildly relativistic winds with $\beta = 0.1$–$0.3c$ indicate the Eddington ratio $\Gamma = 0.2$–2.6.

ACKNOWLEDGEMENTS

This work was partly supported by the Square Kilometer Array pre-research funding from the Ministry of Science and Technology of the People's Republic of China (2018YFA0404603) and the Chinese Academy of Sciences (CAS; No. 114231KYSB20170003). EN acknowledges financial support from the agreement ASI-INAF n.2017-14-H.0. LF acknowledges the support from National Natural Science Foundation of China (NSFC; Grant Nos. 11822303, 11773020, and 11421303) and Shandong Provincial Natural Science Foundation, China (JQ201801). The EVN is a joint facility of independent European, African, Asian, and North American radio astronomy institutes. Scientific results from data presented in this publication are derived from the following EVN project code(s): EY027. e-VLBI research infrastructure in Europe is supported by the European Union's Seventh Framework Programme (FP7/2007-2013) under grant agreement number RI-261525 NEXPReS. e-MERLIN is a National Facility operated by the University of Manchester at Jodrell Bank Observatory on behalf of STFC. The research leading

to these results has received funding from the European Commission Horizon 2020 Research and Innovation Programme under grant agreement no. 730562 (RadioNet). This work has made use of data from the European Space Agency (ESA) mission *Gaia* (https://www.cosmos.esa.int/gaia), processed by the *Gaia* Data Processing and Analysis Consortium (DPAC; https://www.cosmos.esa.int/web/gaia/dpac/consortium). Funding for the DPAC has been provided by national institutions, in particular the institutions participating in the *Gaia* Multilateral Agreement. This research has made use of the NASA/IPAC Extragalactic Database (NED), which is operated by the Jet Propulsion Laboratory, California Institute of Technology, under contract with the National Aeronautics and Space Administration. This research has made use of NASA's Astrophysics Data System Bibliographic Services.

DATA AVAILABILITY

The correlation data of the EVN experiment EY027 are available to the public in the EVN data archive. The calibrated visibility data and the final image files underlying this article will be shared on reasonable request to the corresponding author.

REFERENCES

Abramowicz M. A., Ellis G. F. R., Lanza A., 1990, ApJ, 361, 470
Alexandroff R. et al., 2012, MNRAS, 423, 1325
An T., Baan W. A., 2012, ApJ, 760, 77
An T., Baan W. A., Wang J.-Y., Wang Y., Hong X.-Y., 2013, MNRAS, 434, 3487
Bell E. F., 2003, ApJ, 586, 794
Bischetti M. et al., 2019, A&A, 628, A118
Blandford R. D., Payne D. G., 1982, MNRAS, 199, 883
Blandford R. D., Znajek R. L., 1977, MNRAS, 179, 433
Blandford R., Meier D., Readhead A., 2019, ARA&A, 57, 467
Boissay-Malaquin R., Danehkar A., Marshall H. L., Nowak M. A., 2019, ApJ, 873, 29
Briggs D. S., 1995, BAAS, 27, 1444
Chabrier G., 2003, PASP, 115, 763
Chen H. et al., 2020, A&A, 638, A113
Condon J. J., Condon M. A., Gisler G., Puschell J. J., 1982, ApJ, 252, 102
Fan L., Han Y., Nikutta R., Drouart G., Knudsen K. K., 2016, ApJ, 823, 107
Fan L., Jones S. F., Han Y., Knudsen K. K., 2017, PASP, 129, 124101
Fan L., Knudsen K. K., Han Y., Tan Q.-H., 2019, ApJ, 887, 74
Fiore F. et al., 2017, A&A, 601, A143
Frey S., Paragi Z., Gabányi K. É., An T., 2016, MNRAS, 455, 2058
Gaia Collaboration, 2018, A&A, 616, A1
Giroletti M., Panessa F., Longinotti A. L., Krongold Y., Guainazzi M., Costantini E., Santos-Lleo M., 2017, A&A, 600, A87
Greisen E. W., 2003, in Heck A., ed., Astrophysics and Space Science Library, Vol. 285, Information Handling in Astronomy: Historical Vistas. Kluwer, Dordrecht, p. 109
Hamann F., Chartas G., Reeves J., Nardini E., 2018, MNRAS, 476, 943
Han Y., Han Z., 2012, ApJ, 749, 123
Han Y., Han Z., 2014, ApJS, 215, 2
Han Y., Han Z., 2019, ApJS, 240, 3
Keimpema A. et al., 2015, Exp. Astron., 39, 259
Kettenis M., van Langevelde H. J., Reynolds C., Cotton B., 2006, in Gabriel C., Arviset C., Ponz D., Enrique S., eds, ASP Conf. Ser. Vol. 351, Astronomical Data Analysis Software and Systems XV. Astron. Soc. Pac., San Francisco, p. 497
Kormendy J., Ho L. C., 2013, ARA&A, 51, 511
Kunert-Bajraszewska M., Gawroński M. P., Labiano A., Siemiginowska A., 2010, MNRAS, 408, 2261
Lamastra A., Menci N., Fiore F., Antonelli L. A., Colafrancesco S., Guetta D., Stamerra A., 2017, A&A, 607, A18
Letawe Y., Letawe G., Magain P., 2010, MNRAS, 403, 2088
Matzeu G. A., Reeves J. N., Braito V., Nardini E., McLaughlin D. E., Lobban A. P., Tombesi F., Costa M. T., 2017, MNRAS, 472, L15
Mohan P., Mangalam A., 2015, ApJ, 805, 91
Nardini E. et al., 2015, Science, 347, 860
Nims J., Quataert E., Faucher-Giguère C.-A., 2015, MNRAS, 447, 3612
O'Brien P. T., Reeves J. N., Simpson C., Ward M. J., 2005, MNRAS, 360, L25
Panessa F., Baldi R. D., Laor A., Padovani P., Behar E., McHardy I., 2019, Nat. Astron., 3, 387
Petrov L., Kovalev Y. Y., Fomalont E. B., Gordon D., 2006, AJ, 131, 1872
Pushkarev A. B., Kovalev K. K., Lister M. L., Savolainen T., 2017, MNRAS, 468, 4992
Reeves J. N., O'Brien P. T., Vaughan S., Law-Green D., Ward M., Simpson C., Pounds K. A., Edelson R., 2000, MNRAS, 312, L17
Reeves J. N., Braito V., Nardini E., Lobban A. P., Matzeu G. A., Costa M. T., 2018, ApJ, 854, L8
Reeves J. N., Braito V., Chartas G., Hamann F., Laha S., Nardini E., 2020, ApJ, 895, 37
Romero-Cañizales C., Pérez-Torres M. A., Alberdi A., 2012, MNRAS, 422, 510
Shakura N. I., Sunyaev R. A., 1973, A&A, 500, 33
Sharma M., Nath B. B., 2012, ApJ, 750, 55
Shepherd M. C., Pearson T. J., Taylor G. B., 1994, BAAS, 26, 987
Simpson C., Ward M., O'Brien P., Reeves J., 1999, MNRAS, 303, L23
Tchekhovskoy A., Narayan R., McKinney J. C., 2011, MNRAS, 418, L79
Tombesi F., 2016, Astron. Nachr., 337, 410
Tombesi F., Meléndez M., Veilleux S., Reeves J. N., González-Alfonso E., Reynolds C. S., 2015, Nature, 519, 436
Torres C. A. O., Quast G. R., Coziol R., Jablonski F., de la Reza R., Lépine J. R. D., Gregório-Hetem J., 1997, ApJ, 488, L19
Varenius E. et al., 2016, A&A, 593, A86
Varenius E. et al., 2019, A&A, 623, A173
Weiler K. W., Panagia N., Montes M. J., Sramek R. A., 2002, ARA&A, 40, 387
Yang J., An T., Zheng F., Baan W. A., Paragi Z., Mohan P., Zhang Z., Liu X., 2019, MNRAS, 482, 1701
Yang J., Paragi Z., An T., Baan W. A., Mohan P., Liu X., 2020a, MNRAS, 494, 1744
Yang J., Gurvits L. I., Paragi Z., Frey S., Conway J. E., Liu X., Cui L., 2020b, MNRAS, 495, L71
Yun M. S., Reddy N. A., Scoville N. Z., Frayer D. T., Robson E. I., Tilanus R. P. J., 2004, ApJ, 601, 723
Zakamska N. L., Greene J. E., 2014, MNRAS, 442, 784

This paper has been typeset from a TEX/LATEX file prepared by the author.